Published in final edited form as:
Phys Med Biol. 2008 October 7; 53(19): 5371–5383. doi:10.1088/0031-9155/53/19/007.

Improving the quantitative accuracy of optical-emission computed tomography by incorporating an attenuation correction: application to HIF1 imaging

E Kim, **J Bowsher**, **A S Thomas**, **H Sakhalkar**, **M Dewhirst**, and **M Oldham**
Department of Radiation Oncology, Duke University Medical Center, Durham, NC, USA

Abstract

Optical computed tomography (optical-CT) and optical-emission computed tomography (optical-ECT) are new techniques for imaging the 3D structure and function (including gene expression) of whole unsectioned tissue samples. This work presents a method of improving the quantitative accuracy of optical-ECT by correcting for the 'self'-attenuation of photons emitted within the sample. The correction is analogous to a method commonly applied in single-photon-emission computed tomography reconstruction. The performance of the correction method was investigated by application to a transparent cylindrical gelatin phantom, containing a known distribution of attenuation (a central ink-doped gelatine core) and a known distribution of fluorescing fibres. Attenuation corrected and uncorrected optical-ECT images were reconstructed on the phantom to enable an evaluation of the effectiveness of the correction. Significant attenuation artefacts were observed in the uncorrected images where the central fibre appeared ~24% less intense due to greater attenuation from the surrounding ink-doped gelatin. This artefact was almost completely removed in the attenuation-corrected image, where the central fibre was within ~4% of the others. The successful phantom test enabled application of attenuation correction to optical-ECT images of an unsectioned human breast xenograft tumour grown subcutaneously on the hind leg of a nude mouse. This tumour cell line had been genetically labelled (pre-implantation) with fluorescent reporter genes such that all viable tumour cells expressed constitutive red fluorescent protein and hypoxia-inducible factor 1 transcription-produced green fluorescent protein. In addition to the fluorescent reporter labelling of gene expression, the tumour microvasculature was labelled by a light-absorbing vasculature contrast agent delivered *in vivo* by tail-vein injection. Optical-CT transmission images yielded high-resolution 3D images of the absorbing contrast agent, and revealed highly inhomogeneous vasculature perfusion within the tumour. Optical-ECT emission images yielded high-resolution 3D images of the fluorescent protein distribution in the tumour. Attenuation-uncorrected optical-ECT images showed clear loss of signal in regions of high attenuation, including regions of high perfusion, where attenuation is increased by increased vascular ink stain. Application of attenuation correction showed significant changes in an apparent expression of fluorescent proteins, confirming the importance of the attenuation correction. In conclusion, this work presents the first development and application of an attenuation correction for optical-ECT imaging. The results suggest that successful attenuation correction for optical-ECT is feasible and is essential for quantitatively accurate optical-ECT imaging.

1. Introduction

Optical computed tomography (optical-CT) and optical-emission computed tomography (optical-ECT) can be considered as the optical analogues of x-ray CT and single-photon-emission computed tomography (SPECT). Optical-CT has been utilized for high-resolution 3D dosimetry in radiation therapy (Gore *et al* 1996, Kelly *et al* 1998, Wolodzko *et al* 1999, Doran *et al* 2001, Oldham *et al* 2001). Optical-ECT was first proposed by Sharpe *et al* as a tool for imaging gene expression via fluorescently labelled antibodies in mouse embryos

(Sharpe *et al* 2002, Sharpe 2003). Sharpe *et al* also demonstrated optical-CT transmission imaging of the distribution of LacZ-expressing cells in the developing mouse brain, where LacZ expression had been labelled with the light absorbing X-gal stain. The optical-CT/ECT combination was further extended by Oldham *et al* (2006) to image the 3D microvasculature structure and viable tumour cell distribution in whole xenograft tumours. High-resolution co-registered images of the 3D microvasculature and viable tumour-cell distribution in ~1 cc unsectioned xenograft tumours that had been transfected to constitutively express red fluorescent protein (RFP) were obtained. Further developments were reported in Oldham *et al* (2007), including a second-generation optical-CT/ECT system with the ability to image unsectioned rodent organs as large as 3 cm with 50 μm resolution. These works have established optical-CT/ECT as promising new tools for 3D imaging of the structure and function (including gene expression) in unsectioned biological tissue.

Several advances have recently occurred improving the technique of optical-CT/ECT imaging. For optical-CT, image acquisition hardware has evolved from laser scanning/ photodiode point detection (Gore *et al* 1996, Maryanski *et al* 1996, Oldham *et al* 2001, 2003, Oldham and Kim 2004) to a telecentric lens coupled CCD camera (Oldham *et al* 2007, 2008). Walls *et al* (2005) and Oldham and Kim (2004) described methods for correcting several reconstruction artefacts in optical-CT. The extension of optical-CT/ECT imaging to biological tissue has necessitated the development of optical clearing techniques (Tuchin 2005), which render the excised tissue samples much more transparent and enable sufficient light penetration to acquire optical-CT/ECT projection images. This is a critical new step, and major advances have been recently reported (Sakhalkar *et al* 2007), including the feasibility to optically clear large tissue samples (>1 cc) while preserving the *in vivo* condition of the stains of interest, including both fluorescing reporter proteins and vascular absorbing contrast agents. The essential mechanism of the optical clearing techniques is to replace intra- and extra-cellular fluids with a fluid of a higher refractive index that matches that of cellular and sub-cellular membranes (Oldham 2007). Homogenizing the refractive index significantly reduces light scattering within the tissues, enabling us to achieve high-resolution 3D imaging with optical-CT/ECT techniques.

Recent data showing co-registered optical-CT/ECT images of fluorescent reporter protein distribution in xenograft tumours indicate that attenuation artefacts can reduce the accuracy of optical-ECT (Oldham *et al* 2008). Attenuation artefacts may arise from two mechanisms. The first mechanism, attenuation of emitted light, occurs when light emitted by proteins fluorescing in the sample are self-absorbed in the sample and fail to contribute to the projection image. The second mechanism, attenuation of excitation light, occurs when the incident excitation light (which causes embedded proteins to fluoresce) is attenuated, causing loss of stimulation of fluorescence. The first of these mechanisms is analogous to the attenuation routinely encountered in SPECT, and a range of analytic and iterative image reconstruction techniques have been proposed to correct for such attenuation. With iterative techniques, attenuation correction is accomplished by modelling attenuation within a matrix that describes projection acquisition and that includes attenuation-survival probabilities (Shepp *et al* 1985, Tsui *et al* 1989). Methods for determining the attenuation-survival probabilities include use of a co-registered x-ray-CT image (Zaidi and Hasegawa 2003, Kinahan *et al* 2003). To date, attenuation correction has not been implemented for optical-ECT. Attenuation artefacts for the second mechanism can be minimized by good experimental design, incorporating simultaneous illumination of the sample from multiple judicious orientations. This work focuses on developing a correction for the more significant first mechanism of attenuation. We propose and demonstrate the first effective correction for self-absorbed attenuation in optical-ECT. The method computes attenuation-survival probabilities from the attenuation map obtained from a pre-requisite optical-CT image of the

sample, and includes these probabilities within iterative ordered-subsets expectation-maximization (OSEM) (Hudson and Larkin 1994) reconstruction of the optical-ECT image.

2. Methods and materials

An overview of the optical-CT and optical-ECT apparatus and imaging techniques is given in section 2.1. The principles and implementation of the new attenuation correction are described in section 2.2. Section 2.3 describes a phantom study designed to verify the basic performance of the attenuation correction method. Section 2.4 describes the application of attenuation correction to optical-ECT images of a xenograft tumour containing fluorescent reporter proteins labelling viable tumour cells (RFP) and hypoxia-inducible factor 1 (HIF1) expression (green fluorescent protein (GFP)).

2.1. Optical-CT/ECT imaging system

The in-house bench top optical-CT/ECT system (figure 1) has been described previously (Oldham *et al* 2007). In summary, an optically cleared tissue sample, encased in a transparent cylindrical agarose gel, is placed on a rotating stage inside an anti-reflection-coated glass aquarium. The aquarium is filled with an index matching fluid to minimize refraction and reflection of incident light on the agarose gel and sample. As the sample rotates, projection images are acquired on a CCD camera coupled to a telecentric lens (TECHSPEC 55–349 telecentric lens system—Edmund Optics Inc., Barrington, NJ), which forms an image on the CCD of light rays that travel parallel to the optic axis within a tolerance of ~0.1°. The projection images are of transmitted light in optical-CT and emitted light in optical-ECT. The application of appropriate filter sets to the incident light sources (FiberLite MH100 metal halide illuminators—Dolan Jenner Industries Inc., Lawrence, MA) enables optical-CT/ECT at different wavelengths.

2.1.1. Optical-CT—In optical-CT (figure 1(A)), a single illuminator is coupled to a uniform backlight (Dolan Jenner Industries Inc., Lawrence, MA) by a liquid optical fibre to provide a diffuse background illumination. Light rays travel from the backlight through the sample, where they experience differential attenuation. These projection images were acquired by an A-102f 12 bit monochrome CCD camera (BaslerVision Technologies, Ahrensburg, Germany). The telecentric lens produces images that accurately reflect parallel-light-ray geometry. In addition, projection images have minimal scatter artefacts and constant magnification over the entire depth of field (eliminating perspective error). An in-house LABVIEW code controls a ‘step-and-image’ acquisition scheme in which the stage makes an incremental rotation after a projection image from the camera is written to disk. The optical-CT images were reconstructed using an in-house software package ‘Image-MAP’ and the ordered-subsets-transmission-reconstruction (OSTR) algorithm (Erdogan and Fessler 2007).

2.1.2. Optical-ECT—In optical-ECT (figure 1(B)), two illuminators are coupled to liquid optical fibres to excite the sample on both sides orthogonal to the optic axis. Appropriate excitation and emission filters are coupled to the light source and telecentric lens, respectively, to enable selective stimulation and imaging of specific fluorofors. The acquisition technique and equipment for optical-ECT are identical to those for optical-CT, except that there is an additional shutter synchronization element that opens VS25S2T1 shutters (Vincent Associates, Rochester, NY) in front of the light sources only during image acquisition to minimize photo-bleaching. Once acquired, a complete set of optical-ECT projection images was reconstructed by using the algorithm described in section 2.2. The attenuation correction was determined from the optical-CT scan, which yields a 3D map of the attenuation within the sample.

2.2. Attenuation correction and iterative reconstruction in optical-ECT

All 3D reconstructions were generated with 'Image-MAP'. This software implemented the reconstruction methods described in this section. The relationship between the projection images and the distribution of sample fluorescence in optical-ECT can be described as a linear system (equation (1)),

$$E_i = \overline{E}\, M_i = \overline{E} \sum_{j=1}^{N_{vox}} S_j \lambda_j P_{ij} \approx \overline{E}\, S_0 \sum_{j=1}^{N_{vox}} \lambda_j P_{ij}, \tag{1}$$

where E_i is the expected value for the energy integrated at detector bin i, $\hat{E}$ is the average energy per detected photon and M_i is the expected number of photons detected at bin i. The quantity M_i is computed as a sum over voxels of the product $S_j \lambda_j P_{ij}$, where S_j is the expected number of excitation photons reaching voxel j, λ_j is the expected number of photons emitted from voxel j per excitation photon reaching voxel j and P_{ij} is the probability that a photon emitted from voxel j is detected at bin i. In general, S_j can differ for different voxels j, because of non-uniform illumination of the sample with excitation light and because of differing attenuation of the excitation light that reaches different voxels. In this work, we omit modelling of these variations and assume equal excitation illumination S_0 of all voxels. The optical-ECT imaging system is designed to accomplish this approximately with a parallel opposed arrangement of excitation illumination sources. (That noted, modelling variations in S_j within image reconstruction may be an important area of future work.) The quantity $\bar{E}$ is the centre of a narrow energy band that contains all detected photons. The band is narrow because fluorescing proteins emit within a narrow band and because energy filters are placed over the detector. The quantity λ_j is proportional to the amount of fluorescing protein in voxel j, and the output of image reconstruction is an estimate of these quantities λ_j.

Multiple acquisition effects can be described within P_{ij}. For example, in SPECT, P_{ij} is sometimes used to describe not only attenuation but also spatial resolution and, less frequently, scatter. Here we use P_{ij} to describe the probability that a photon emitted from voxel j will survive attenuation as it travels towards detector bin i. In reconstructing an attenuation-uncorrected emission image, P is calculated assuming uniform zero attenuation. In reconstructing an attenuation-corrected emission image, P is calculated by using the nonuniform attenuation map obtained from the corresponding optical-CT image. Once P is computed, optical-ECT images are reconstructed, based on the above model, using the OSEM algorithm (Hudson and Larkin 1994).

2.3. Verification of attenuation correction on a known phantom

The effectiveness of the attenuation correction was verified by optical-ECT imaging a gelatin phantom containing a known distribution of attenuation and three identical fluorescent fibres. The phantom consisted of a cylindrical transparent gelatin gel with an attenuating central cuboidal core (1×1 cm^2 in cross section and 3 cm long), orientated with the long axis co-incident with that of the surrounding gel cylinder. This inner core was made attenuating by doping the gel with India ink (method described below). Three identical fluorescent fibres (0.5 mm diameter) were placed in the attenuating core, one central to the core and two in the periphery of the core, at positions corresponding to maximum and minimum attenuation respectively. The fibre in the centre of the core will exhibit significant attenuation in all projection images irrespective of the acquisition angle. The peripheral fibres will exhibit little self-attenuation in some projections, where the detector is on the downstream edge of the light rays, but strong attenuation when on the upstream side. An optical-CT scan of the phantom would reveal the attenuation distribution and the precise

location of the fibres. Knowing the attenuation and fluorescence distribution enables an accurate assessment of the improvement of the optical-ECT image gained from the attenuation correction.

The phantom was constructed by mixing 40 mL of water and 5 g of Difco™ gelatin (Becton, Dickinson and Company, Sparks, MD) in a clear glass vial (4 cm diameter) suitable for imaging. The solution was heated and stirred until the gelatin was completely dissolved. While still fluid, a spectrometer cuvette ($1 \times 1 \times 4$ cm^3) was positioned in the centre of the glass vial, such that it displaced the gelatine solution. The phantom and cuvette were then placed in the refrigerator to cause the gelatine to set around the cuvette. Once the gelatin had set, the cuvette was removed by filling it with hot water, which dissolved a thin layer of the gelatin surrounding the cuvette. The phantom was refrigerated upside down for another 30 min to allow the hollow core to stabilize. The hollow core was then filled with the remainder liquid gelatin that had been doped with India ink. The temperature of the doped liquid gel was kept just above the setting temperature at the time of pouring to preserve the boundary between doped and transparent gelatin. Once the ink-doped gelatin began to solidify, three segments of red fluorescent fibre (Nanoptics, Inc., Gainesville, FL) were placed vertically in the core: one near the centre and two on opposite sides close to the periphery. The phantom was then refrigerated for an additional 30 min.

In preparation for scanning, the phantom was positioned on the rotation stage, and the aquarium was then filled with a 50% glycerol/water solution to minimize refraction of incident light on the edges of the glass vial. 180 optical-CT/ECT projections of the phantom were acquired at 2° increments. Flood-field and dark-field images were acquired prior to placing the sample in the aquarium. The optical-CT and optical-ECT scans were conducted consecutively, without removing the phantom, to ensure accurate co-registration. DSRed2 excitation (558 nm) and emission (583 nm) filters were used to excite and image, respectively, the fluorescent fibres in the optical-ECT scan respectively. The wavelength of the transmission optical-CT scan was selected to match that of the emitted light in optical-ECT, to ensure accurate representation of the attenuation in the optical-ECT image.

The raw transmission and emission projection images were cropped to remove refraction and reflection artefacts at the edges of the vial, and to correct for any detector offset. The projections were also downsized by a factor of 2 to reduce computation time. The images were reconstructed with Image-Map, on a 256×256 grid, maintaining a one-to-one projection-to-reconstruction ratio. The optical-CT and optical-ECT reconstructions utilized 20 iterations of 16-subset OSTR and OSEM, respectively. Attenuation corrected and uncorrected optical-ECT images were reconstructed.

2.4. Application to xenograft tumour images

2.4.1. Tumour preparation—After basic verification through the phantom study, the attenuation correction method was applied to images of a 4T1 xenograft human breast tumour. The 4T1 tumour cells had been double transfected with reporter genes coding for constitutive RFP expression and GFP labelling of the HIF1 gene (Cao *et al* 2005). The tumour cells were injected subcutaneously into the hind leg of a nude mouse, following an IACUC-approved protocol. When the tumour had grown to approximately 1 cm, the tumour microvasculature was stained *in vivo* with a dilute solution of isotonic India ink via tail-vein injection. Five minutes after injection, the mouse was sacrificed and the tumour excised. The tumour was then fixed, set in agarose gel and optically cleared using a fluorescence preserving procedure (Sakhalkar *et al* 2007). Multiple labelling of the tumour as described in this section enabled multiple optical-CT/ECT scans to determine 3D distributions of different biologic parameters. A transmission optical-CT scan would yield images sensitive to the attenuating ink uptake in the microvasculature. Optical-ECT imaging with RFP filters

would yield images of the viable tumour cell burden, as any necrotic or other non-viable tumour regions would not exhibit fluorescence. Optical-ECT imaging with GFP filters would indicate the 3D distribution of HIF1 expression.

2.4.2. Tumour imaging and reconstruction—Two optical-ECT scans (corresponding to GFP and RFP filters) and an optical-CT scan were acquired on the xenograft tumour. 361 projections were acquired at 1° increments for each scan, and the optical-ECT scans were performed first to minimize photobleaching. The DSRed2 (RFP) filter set was used to image the viable tumour distribution, and blue excitation filters and a custom GFP emission filter were used to image the HIF1distribution. Flood-field and dark-field projection images were acquired for the optical-CT scan. The aquarium was filled with a BABBs solution (2:1 ratio of benzyl alcohol:benzyl benzoate) to minimize refraction at the edge of the agarose gel surrounding the tumour.

The raw transmission and emission projection images were cropped and downsized by a factor of 2 to reduce computation time for this feasibility study. Image-MAP was used to reconstruct the three images onto a 512 ×512 grid, again maintaining a one-to-one projection-to-reconstruction ratio. The optical-CT and optical-ECT reconstructions utilized 25 iterations of 16-subset OSTR and OSEM, respectively. Attenuation corrected and uncorrected optical-ECT images were reconstructed for comparison.

3. Results and discussion

3.1. Verification phantom study

Representative projection images of the phantom acquired in both optical-CT and optical-ECT are shown in figure 2. The three fibres are visible in both the transmission (optical-CT) and the emission (optical-ECT) projections, as the fibres can both attenuate light and fluoresce when exposed to appropriate excitation light. The ink-doped core is only visible in the optical-CT projection as it attenuates but has no fluorescence. Central slices of the optical-CT and attenuation uncorrected and corrected optical-ECT images of the phantom were reconstructed using Image-Map (figure 3). The optical-CT transmission reconstruction represents the attenuation map of the phantom (figure 3(A)), where each voxel value is the attenuation coefficient at that voxel. The reconstructed images are consistent with the expected results, showing the three attenuating fibres positioned in the central square (in cross-section) ink-doped attenuating core. In the optical-ECT reconstructions (figures 3 (B) and (C)), only the three fibres are visible as these are the only sources of fluorescent light in the sample. The difference between the attenuation uncorrected and corrected optical-ECT images is not readily apparent in the raw reconstructions (figures 3(B) and (C)) but is clear in the corresponding surface plots (figures 3(E) and (F)). In the uncorrected optical-ECT surface plot (figure 3(E)), the centre fibre appears significantly less intense than the peripheral fibres, even though they are segments of the same fibre and should have identical light output. This artefact is primarily due to varying average path lengths through the attenuating ink of emitted photons for each fibre. Compared to the peripheral fibres, fewer photons emitted from the centre fibre were detected. The attenuation artefact has been essentially removed in the attenuation-corrected optical-ECT image. The corresponding surface plot (figure 3(F)) shows that the attenuation correction significantly levelled the fibre fluorescence intensities.

A region of interest (ROI) analysis was conducted to quantify the improvement netted by the Image-Map attenuation correction. Circular ROIs, 15 voxels in diameter, were established around each fibre in the optical-ECT reconstructed images. To reduce noise in the images, the mean voxel values of the ROIs were calculated and used as standard quantifications of the fibre fluorescence intensities. The values are shown in figure 4, for the left central and

rightmost fibres in figure 3. The intensities varied by 26% in the attenuation-uncorrected image, compared to 4% in the attenuation-corrected image. The attenuation correction equalized the three fibre fluorescence intensities and also increased the values, indicating the importance of the correction. The increase in value does not represent an increase in the measured signal, and thus has no effect on the SNR. The increase does represent the expected signal in the absence of attenuation. A simple consistency calculation can be made by using the attenuation coefficients of the optical-CT transmission image (figure 3(A)). A typical OD is 1.66 cm^{-1}, and with an average path-length of 0.5 cm, a simple exponential decay would indicate an attenuation of a factor of ~2.3. This is very close to the observed factor of ~2.4 between the corrected and uncorrected intensities in figure 4.

3.2. Application to xenograft tumour images

An optical-CT scan was performed to image the attenuation of the ink-stained tumour microvasculature. Two optical-ECT scans were performed to image the viable tumour (RFP) and HIF1 distributions (GFP). Figure 5 shows projection images at a constant projection angle from the three scans. Darker regions in the transmission optical-CT image indicate regions of higher attenuation where less light travels through the sample to reach the detector. High attenuation occurs in regions of dense vascular uptake of absorbing ink, and may also occur due to residual pigmentation or attenuating structures in the tissue. Lighter regions in the emission images indicate regions where increased fluorescent light emitted in the sample reached the detector. Central slices of the projection data from these scans were reconstructed using Image-Map, and are shown in figure 6. The two optical-ECT images were reconstructed with and without attenuation correction respectively.

In the reconstructed tomographic central slice images, high voxel intensities correspond to high attenuation in the optical-CT image and high fluorescence in the optical-ECT images. The arrows in figure 6 indicate regions of high attenuation in the optical-CT image. The corresponding regions in the attenuation-uncorrected optical-ECT RFP images have apparent low fluorescence, which is in contrast to the expectation that highly perfused regions (as indicated by high vascular ink attenuation in the optical-CT image) would contain significant viable tumour burden. In the attenuation-corrected RFP images, increased fluorescence is observed in these regions of expected higher tumour burden. In the uncorrected GFP image, HIF1 expression is observed to be especially prevalent in the periphery of the tumour. However after attenuation correction, a greater expression is observed throughout the central region of the tumour with hot spots and heterogeneity of the expression apparent within the central region. A detailed interpretation is difficult without a full understanding of the role of auto-fluorescence in the tumour. This is beyond the scope of the present study which aims to demonstrate the feasibility and significance of an attenuation correction in optical-ECT. In addition, significant attenuation of the excitation light could produce artefacts. This effect is the subject of a further investigation.

4. Conclusions

An attenuation correction method was successfully developed and applied to optical-ECT imaging that corrects for the attenuation of light emitted within the sample. The basic performance of the method was verified by a phantom study, and the method was subsequently applied to optical-ECT images of a xenograft tumour that was genetically engineered for constitutive RFP expression and GFP labelling of HIF1 gene expression. Optical-CT transmission imaging of the tumour revealed significant variation in vasculature perfusion. The presence of attenuating contrast in the microvasculature clearly affected the reconstructed fluorescence distributions and therefore the apparent viable tumour burden (RFP) and HIF1 expression (GFP). Application of the attenuation correction boosted the apparent viable tumour burden in regions of high perfusion and also significantly altered the

apparent HIF1 distribution. While a detailed interpretation of these effects requires a fuller understanding of auto-fluorescence (subject to further study), the significance of the attenuation correction for optical-ECT imaging in xenograft tumours is clear in the data presented. This work represents the first attempt we are aware of to include such a correction for optical-ECT imaging. While this work demonstrates the potential of optical-ECT to image gene expression, it should also be feasible to obtain quantitative images of the distribution of any analyte (e.g. drug delivery) which possess fluorescent absorptive properties.

References

1. Cao Y, Li CY, Moeller BJ, Yu D, Zhao Y, Dreher MR, Shan S, Dewhirst MW. Observation of incipient tumour angiogenesis that is independent of hypoxia and hypoxia inducible factor-1 activation. Cancer Res. 2005; 65:5498–5505. [PubMed: 15994919]
2. Chang LT. A method for attenuation correction in radionuclide computed tomography. IEEE Trans. Nucl. Sci. 1978; 25:638–643.
3. Doran SJ, Koerkamp KK, Bero MA, Jenneson P, Morton EJ, Gilboy WB. A CCD-based optical CT scanner for high-resolution 3D imaging of radiation dose distributions: equipment specifications, optical simulations and preliminary results. Phys. Med. Biol. 2001; 46:3191–3213. [PubMed: 11768500]
4. Erdogan H, Fessler JA. Ordered subsets algorithms for transmission tomography. Phys. Med. Biol. 2007; 44:2835–2851. [PubMed: 10588288]
5. Gore JC, Ranade M, Maryanski MJ, Schulz RJ. Radiation dose distributions in three dimensions from tomographic optical density scanning of polymer gels: I. Development of an optical scanner. Phys. Med. Biol. 1996; 41:2695–2704. [PubMed: 8971963]
6. Hudson HM, Larkin RS. Accelerated image reconstruction using ordered subsets of projection data. IEEE Trans. Med. Imaging. 1994; 13:601–609. [PubMed: 18218538]
7. Kelly RG, Jordan KJ, Battista JJ. Optical CT reconstruction of 3D dose distributions using the ferrous-benzoic-xylenol (FBX) gel dosimeter. Med. Phys. 1998; 25:1741–1750. [PubMed: 9775382]
8. Kinahan PE, Hasegawa BH, Beyer T. X-ray-based attenuation correction for positron emission tomography/computed tomography scanners. Semin. Nucl. Med. 2003; 33:166–179. [PubMed: 12931319]
9. Krstajic N, Doran SJ. Focusing optics of a parallel beam CCD optical tomography apparatus for 3-D radiation gel dosimetry. Phys. Med. Biol. 2006; 51:2055–2075. [PubMed: 16585845]
10. Maryanski MJ, Zastavker YZ, Gore JC. Radiation dose distributions in three dimensions from tomographic optical density scanning of polymer gels: II. Optical properties of the BANG polymer gel. Phys. Med. Biol. 1996; 41:2705–2717. [PubMed: 8971964]
11. Maxwell PH, Dachs GU, Gleadle JM, Nicholls LG, Harris AL, Stratford IJ, Hankinson O, Pugh CW, Ratcliffe PJ. Hypoxia-inducible factor-1 modulates gene expression in solid tumours and influences both angiogenesis and tumour growth. Proc. Natl Acad. Sci. 1997; 94:8104–8109. [PubMed: 9223322]
12. Moeller BJ, Cao Y, Vujaskovic Z, Li CY, Haroon ZA, Dewhirst MW. The relationship between hypoxia and angiogenesis. Semin. Radiat. Oncol. 2004; 14:215–221. [PubMed: 15254864]
13. Oldham M, Kim L. Optical-CT gel-dosimetry. II: Optical artifacts and geometrical distortion. Med. Phys. 2004; 31:1093–1104. [PubMed: 15191297]
14. Oldham M, Sakhalkar H, Oliver T, Johnson GA, Dewhirst M. Optical clearing of unsectioned specimens for 3D imaging via optical transmission and emission tomography. J. Biomed. Opt. 2008; 13 021113.
15. Oldham M, Sakhalkar H, Oliver T, Wang YM, Kirpatrick J, Cao Y, Badea C, Johnson GA, Dewhirst M. Three-dimensional imaging of xenograft tumours using optical computed and emission tomography. Med. Phys. 2006; 33:3193–3202. [PubMed: 17022212]

16. Oldham M, Sakhalkar H, Wang YM, Guo P, Oliver T, Bentley R, Vujaskovic Z, Dewhirst M. Three dimensional imaging of whole rodent organs using optical computed and emission tomography. J. Biomed. Opt. 2007; 12 014009.

17. Oldham M, Siewerdsen JH, Kumar S, Wong J, Jaffray DA. Optical-CT gel-dosimetry: I. Basic investigations. Med. Phys. 2003; 30:623–634. [PubMed: 12722814]

18. Oldham M, Siewerdsen JH, Shetty A, Jaffray DA. High resolution gel-dosimetry by optical-CT and MR scanning. Med. Phys. 2001; 28:1436–1445. [PubMed: 11488576]

19. Sakhalkar HS, Dewhirst M, Oliver T, Cao Y, Oldham M. Functional imaging in bulk tissue specimens using optical emission tomography: fluorescence preservation during optical clearing. Phys. Med. Biol. 2007; 52:2035–2054. [PubMed: 17404454]

20. Sharpe J. Optical projection tomography as a new tool for studying embryo anatomy. J. Anat. 2003; 202:175–181. [PubMed: 12647867]

21. Sharpe J, Ahlgren U, Perry P, Hill B, Ross A, Hecksher-Sorensen J, Baldock R, Davidson D. Optical projection tomography as a tool for 3D microscopy and gene expression studies. Science. 2002; 296:541–545. [PubMed: 11964482]

22. Shepp LA, Vardi Y, Kaufman L. A statistical model for positron emission tomography. J. Am. Stat. Soc. 1985; 80:8–20.

23. Tsui BMW, Gullberg GT, Edgerton ER, Ballard JG, Perry JR, McCartney WH, Berg J. Correction of nonuniform attenuation in cardiac SPECT imaging. J. Nucl. Med. 1989; 30:497–507. [PubMed: 2786944]

24. Tuchin VV. Optical clearing of tissues and blood using the immersion method. J. Phys. D: Appl. Phys. 2005; 38:2497–2518.

25. Walls JR, Sled JG, Sharpe J, Henkelman RM. Correction of artefacts in optical projection tomography. Phys. Med. Biol. 2005; 50:4645–4665. [PubMed: 16177495]

26. Wolodzko JG, Marsden C, Appleby A. CCD imaging for optical tomography of gel radiation dosimeters. Med. Phys. 1999; 26:2508–2513. [PubMed: 10587241]

27. Zaidi H, Hasegawa B. Determination of the attenuation map in emission tomography. J. Nucl. Med. 2003; 44:291–315. [PubMed: 12571222]

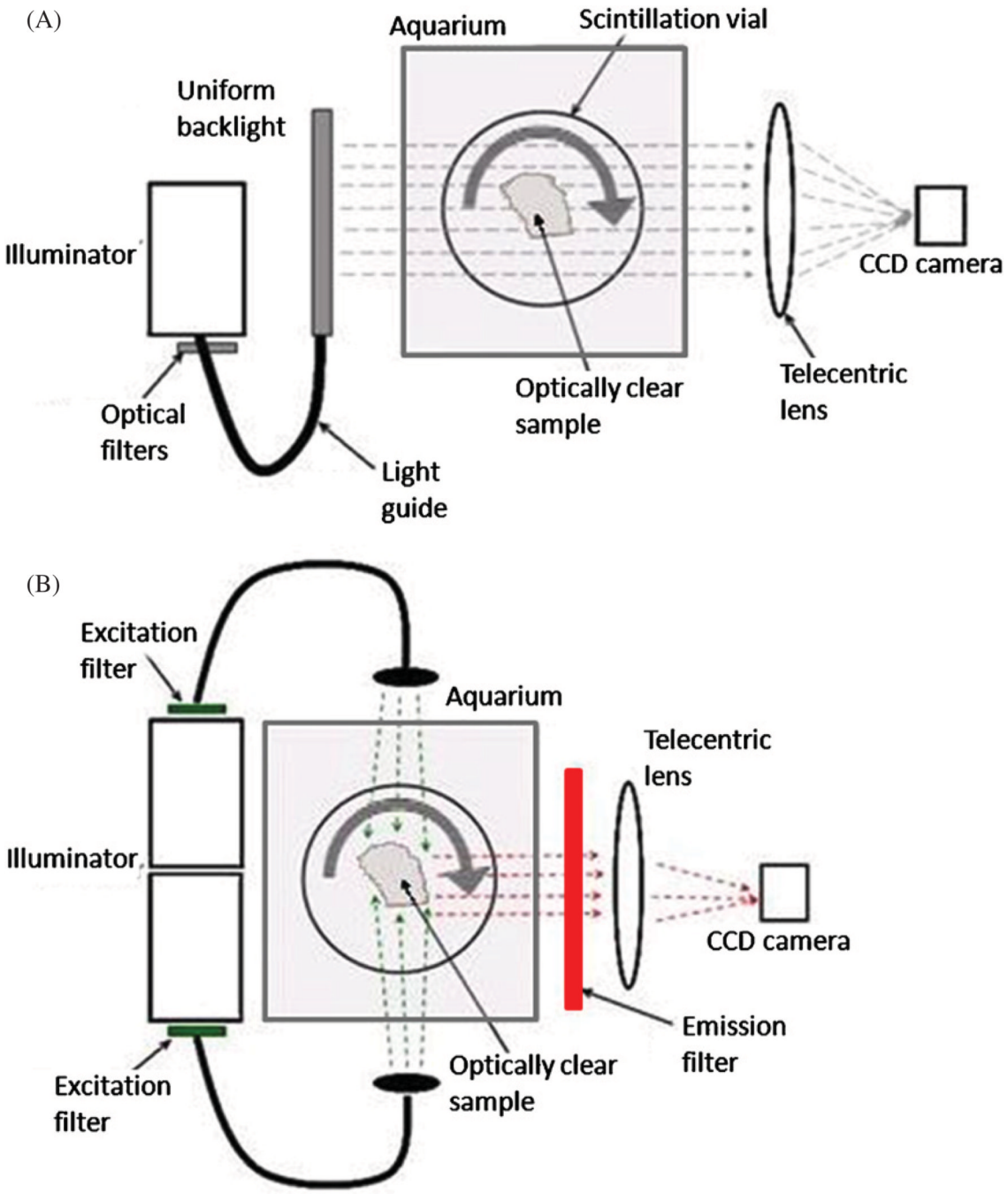

Figure 1.

Simplified schematic of the in-house optical-CT/ECT system. (A) Optical-CT is the optical analogue of x-ray CT. Light is transmitted from a uniform backlight through an optically clear sample, and the resulting projection images are collected by a telecentric lens–CCD camera optical chain. (B) Optical-ECT is the optical analogue of SPECT. Proteins within the sample are stimulated to fluoresce by excitation light sources normal to the imaging axis. Appropriate narrow-bandwidth filters are used for selection of excitation light and collection of emitted light. Emission images are collected using the same imaging components as in (A).

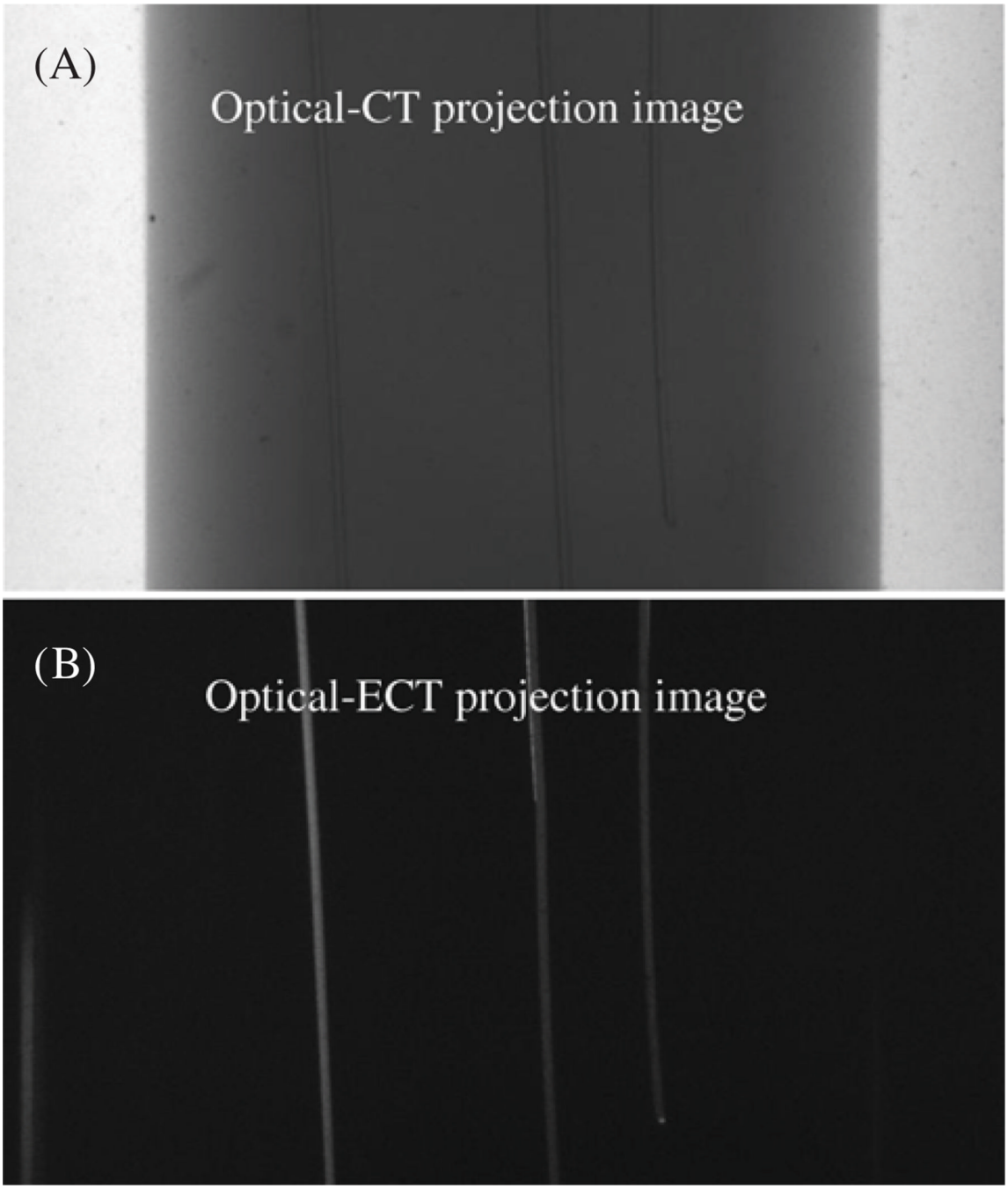

Figure 2.
(A) Optical-CT projection image of the phantom. The ink-doped vertical core containing three fluorescent fibres are visible, although at the optical-CT wavelength the fibres are absorbing and not fluorescing. (B) Optical-ECT projection image of the phantom. Only the three fluorescing fibres are visible as there is no fluorescence in the attenuating gel.

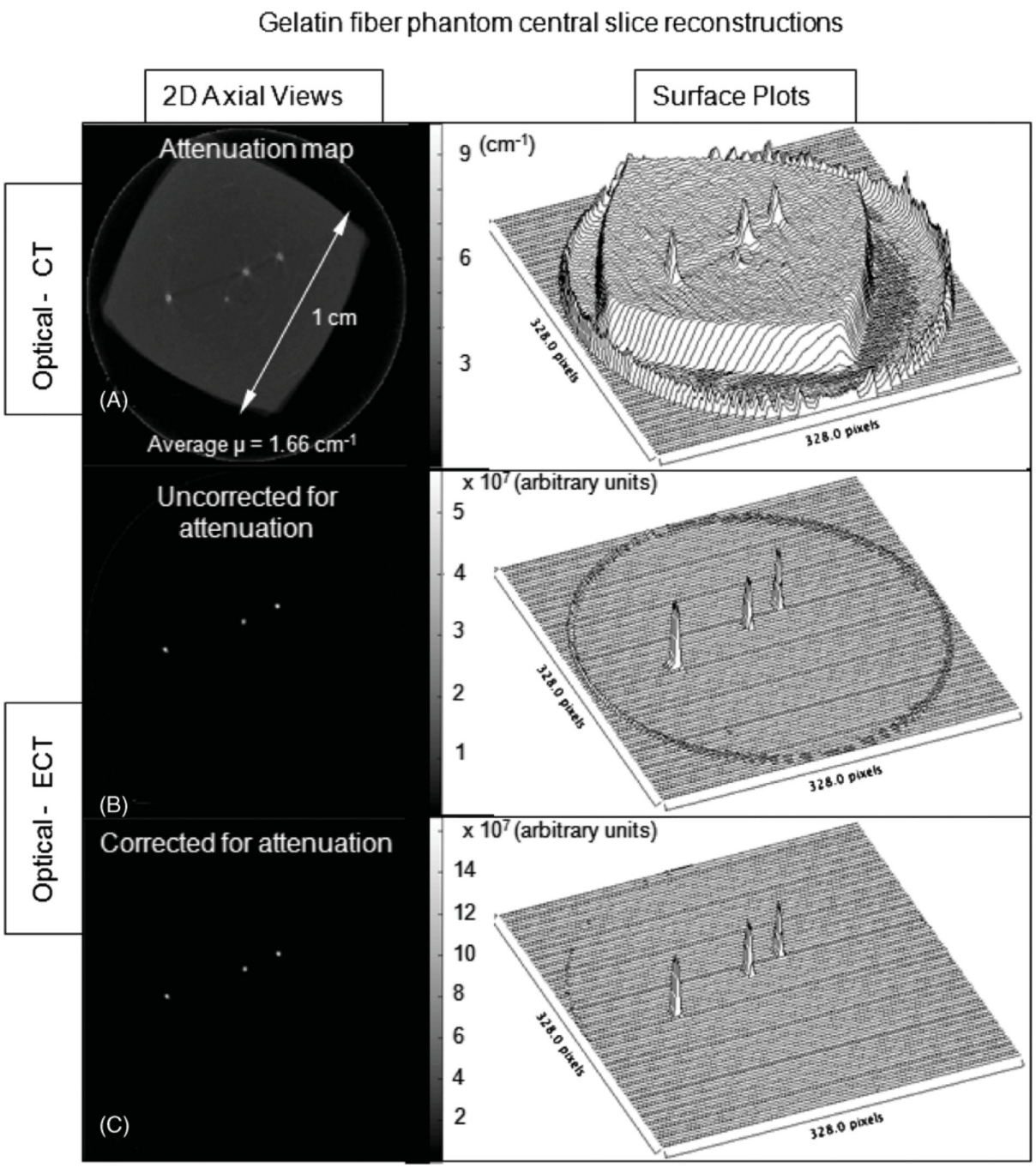

Figure 3.

Central slice reconstructions obtained from Image-Map of the phantom containing known distribution of attenuation and fluorescing fibres. (A) Optical-CT, showing the square outline of the attenuating ink-doped central core, (B) attenuation-uncorrected optical-ECT and (C) attenuation-corrected optical-ECT images of the phantom. The reconstructed optical-CT image (A) is the attenuation map used to calculate the attenuation correction applied in (C). In (B) and (C), only the three fibres are visible as there are no other fluorofors in the sample.

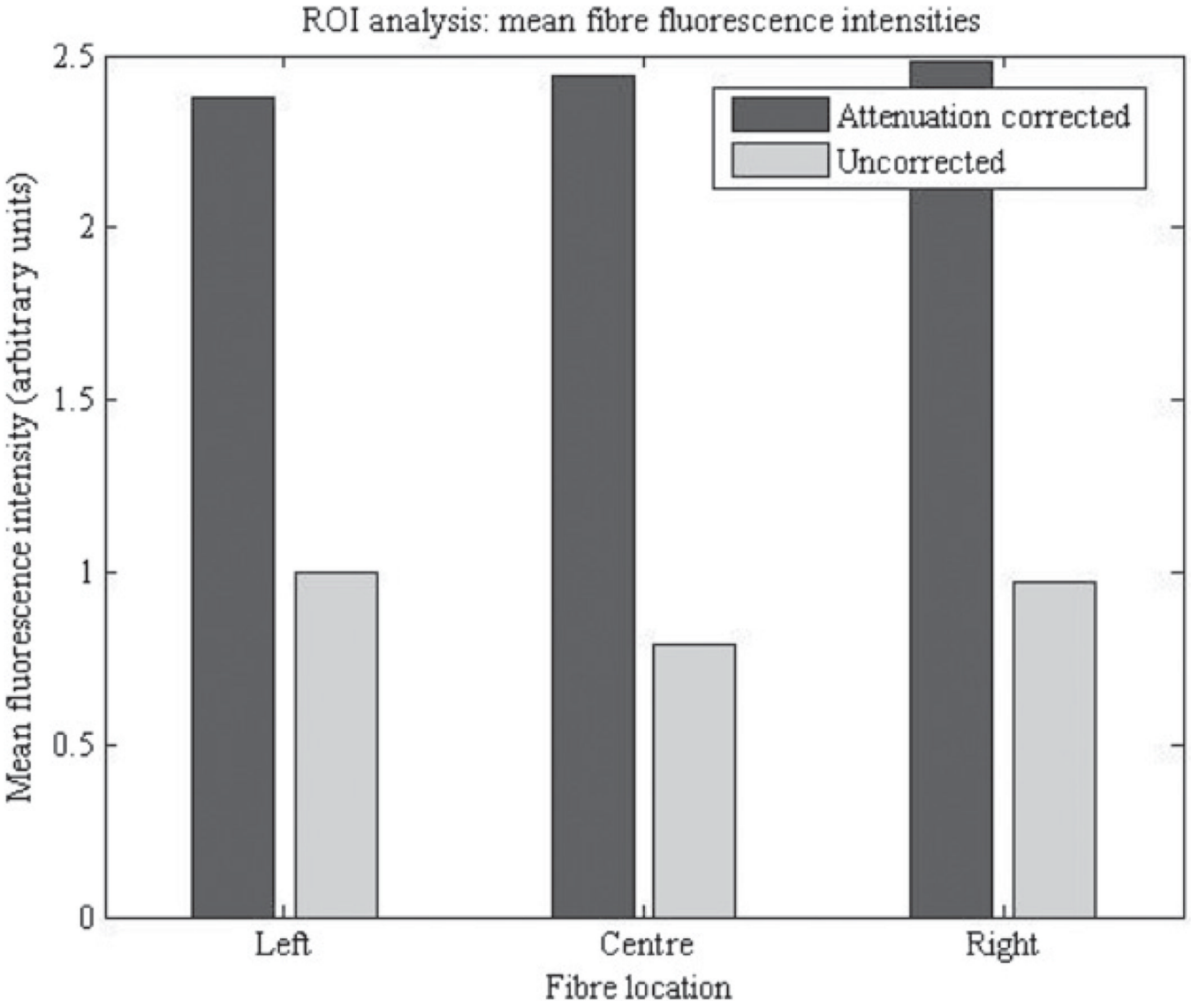

Figure 4.

Mean fibre fluorescence intensities in the attenuation corrected and uncorrected phantom reconstructions. ROI analysis shows that the fluorescence intensities differed by as much as 26% in the attenuation-uncorrected image and only 4% in the attenuation-corrected image.

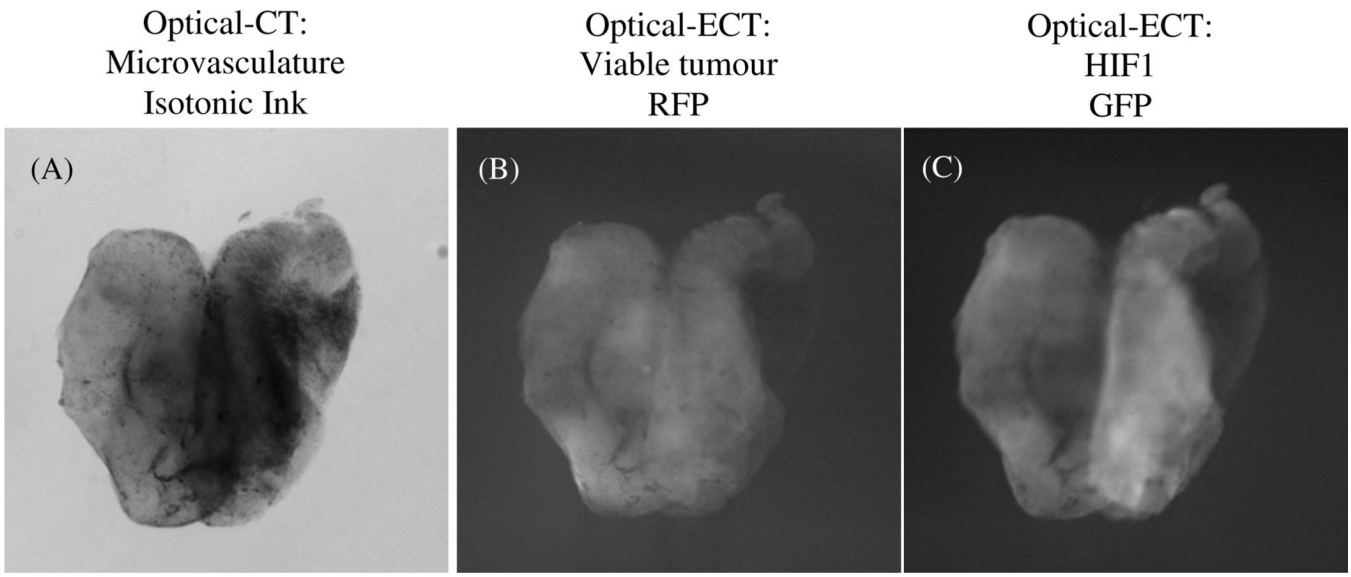

Figure 5.
Projection images of a 4T1 breast xenograft tumour from (A) optical-CT, (B) optical-ECT with a DSRed2 filter set and (C) optical-ECT with an HIF1 filter set (A) dark regions shows the ink-stained tumour microvasculature, (B) light regions show the RFP-expressing viable tumour cell distribution and (C) light regions show the GFP-labelled HIF1 distribution.

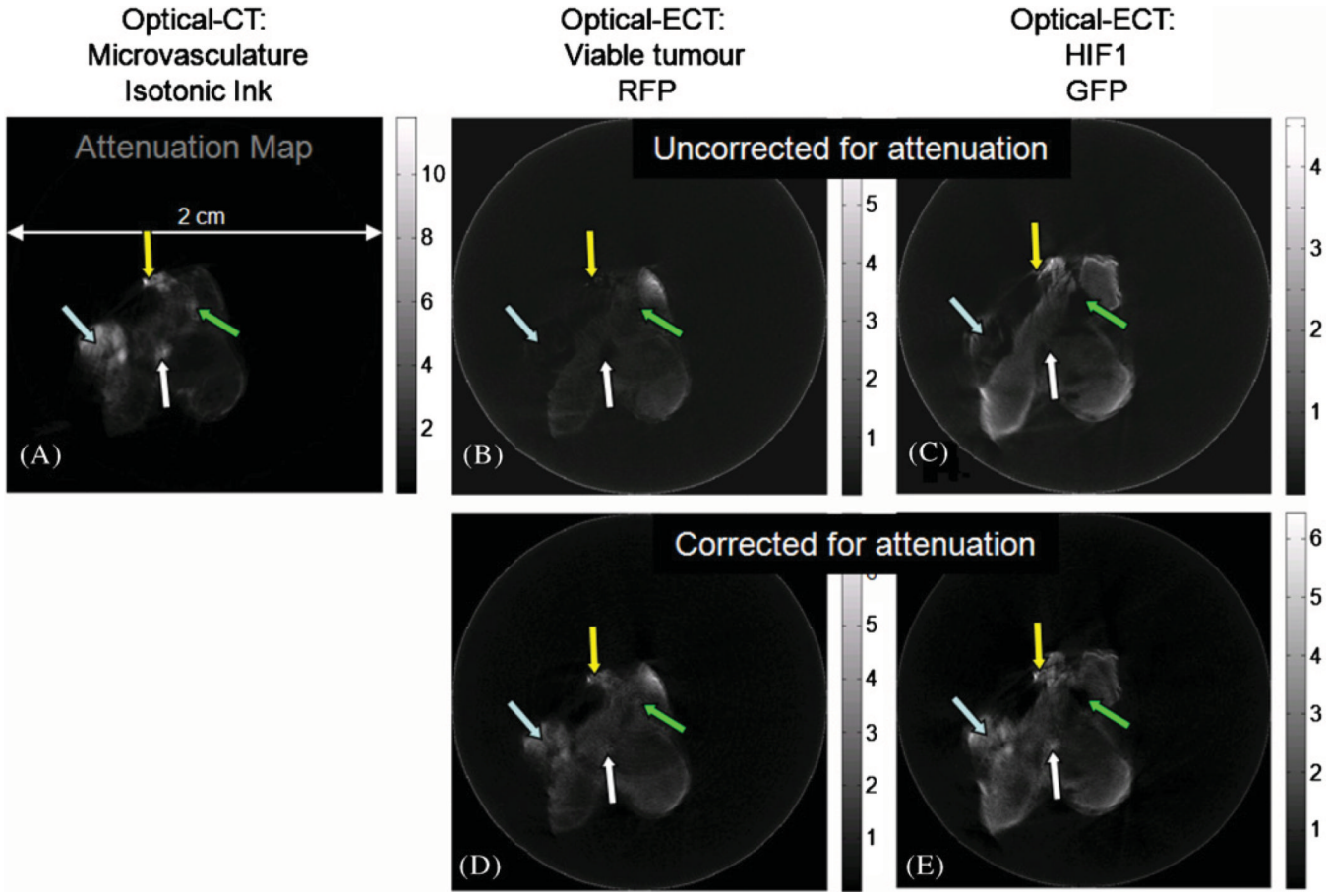

Figure 6.

Central slice tomographic reconstructions of the projection data illustrated in figure 5. (A) The attenuation map from the optical-CT data was used as the basis for the attenuation correction. (B)–(C) Attenuation-uncorrected RFP and GFP optical-ECT reconstructed images, respectively. (D)–(E) Attenuation-corrected RFP and GFP optical-ECT reconstructed images, respectively. The arrows point out regions of high attenuation in (A) that were significantly affected by the attenuation correction.